Preprints.org

Article

Not peer-reviewed version

Dimensionality-Reduction Regulation of C@M-$Zn_2SnO_4(H^+)$ for High-Capacity and Durable Lithium-Ion Battery Anodes

Zhen Meng , YuanYuan Jiang , HengLe Si , JiCun Zheng , HongGang Sun * , GuoQiang Liu *

Posted Date: 13 May 2026

doi: 10.20944/preprints202605.0890.v1

Keywords: Zn_2SnO_4 anode; precision chemical synthesis; dimensionality reduction; nanocompo-sites; lithium-ion batteries

Preprints.org is a free multidisciplinary platform providing preprint service that is dedicated to making early versions of research outputs permanently available and citable. Preprints posted at Preprints.org appear in Web of Science, Crossref, Google Scholar, Scilit, Europe PMC, OpenAlex.

Copyright: This open access article is published under a Creative Commons CC BY 4.0 license, which permit the free download, distribution, and reuse, provided that the author and preprint are cited in any reuse.

Preprints.org (www.preprints.org) | NOT PEER-REVIEWED | Posted: 13 May 2026 doi:10.20944/preprints202605.0890.v1

Disclaimer/Publisher's Note: The statements, opinions, and data contained in all publications are solely those of the individual author(s) and contributor(s) and not of MDPI and/or the editor(s). MDPI and/or the editor(s) disclaim responsibility for any injury to people or property resulting from any ideas, methods, instructions, or products referred to in the content.

Article

Dimensionality-Reduction Regulation of C@M-Zn_2SnO_4(H^+) for High-Capacity and Durable Lithium-Ion Battery Anodes

Zhen Meng [1,2], YuanYuan Jiang [1], HengLe Si [1], JiCun Zheng [1], HongGang Sun [1,*] and Guo-Qiang Liu [2,*]

[1] School of Airspace Science and Engineering, Shandong University

[2] School of Future Technology, Shandong University

* Correspondence: ie@wh.sdu.edu.cn; gqliu@sdu.edu.cn

Abstract

Zn_2SnO_4 is a promising anode for lithium-ion batteries owing to its high theoretical capacity, yet its pratical utilization is severely limited by sluggish reaction kinetics, large volume expansion, and unstable electrode/electrolyte interfaces. Here, we introduce a dimensionality-reduction strategy that simultaneously boosts capacity and cycling stability. Through surfactant-directed crystal growth, acid-etching reconstruction, and hydrothermal carbon coating, compact Zn_2SnO_4 octahedra are controllably transformed into sheet-assembled structures and finally into a core–shell composite with a continuous carbon layer (C@M-Zn_2SnO_4 (H^+)). The continuous structural evolution shortens Li^+ diffusion paths, buffers mechanical stress, and stabilizes the solid-electrolyte interphase without altering the intrinisic lithium-storage mechanism of Zn_2SnO_4. As a result, the optimized C@M-Zn_2SnO_4 (H^+) electrode delivers a reversible capacity of 650 mAh g^{-1} after activation and retains 620 mAh g^{-1} after 600 cycles at 200 mA g^{-1}, with Coulombic efficiency approaching 100% throughout. This work demonstrates that dimensionality-reduction-assisted structural engineering is an effective strategy for developing high-capacity, long-cycle-life anode materials.

Keywords: Zn_2SnO_4 anode; precision chemical synthesis; dimensionality reduction; nanocomposites; lithium-ion batteries

1. Introduction

The rapid expansion of electric transportation and renewable-energy systems has spurred the damand for lithium-ion batteries (LIBs) with higher energy density and extended lifespans [1–6]. However, the practical energy density of current LIBs is still constrained by the limited capacity of commercial graphite anodes, whose theoretical specific capacity is only 372 mAh g^{-1} [7,8]. Developing alternative anode materials with higher capacity while maintaining structural stability during long-term cycling is therefore of great importance [9,11,12].

Among various candidates, Zn_2SnO_4, has attracted considerable attention as a Sn-Zn-based composite oxide because of its high theoretical capacity (1231 mAh g^{-1}), [12,13] low cost, and abundant elemental resource. Nevertheless, its practical application remains hindered by sluggish reaction kinetics, large volume variation, and unstable electrode/electrolyte interfaces [9,14–16]. During repeated lithiation/delithiation, Zn_2SnO_4 undergoes complex conversion and alloying reactions, which generate severe internal stress, particle pulverization, electrical disconnection, and continuous interfacial side reactions [14,15]. These issues usually lead to low initial Coulombic efficiency, aggravated polarization, rapid capacity decay and poor cycling durability [16]. Thus, for Zn_2SnO_4 anodes, the central challenge lies not only in utilizing their high capacity, but in reconciling high-capacity lithium storage with structural and interfacial stability [9,12,16].

© 2026 by the author(s). Distributed under a Creative Commons CC BY license.

Preprints.org (www.preprints.org) | NOT PEER-REVIEWED | Posted: 13 May 2026 doi:10.20944/preprints202605.0890.v1

To address these issue, extensive efforts have focused on nanostructure design and carbon modification [16,17]. Constructing nanosheets, porous frameworks, or hierarchical structures can shorten Li^+ diffusion pathways and alleviate lithiation-induced strain, [18,19] whereas carbon incorporation can enhance electronic conductivity and suppress direct electrolyte attack [20,21]. Despite these advances, most reported strategies improve only part of the problem, because the electrochemical instability of Zn_2SnO_4 originates from the coupling of bulk transport limitation, internal stress accumulation, and interface deterioration [22,23]. In particular, increasing structural openness may accelerate ion transport but also expose more reactive surface to the electrolyte, while simple carbon coating may stabilize the surface without fundamentally relieving diffusion limitation or stress concentration in compact particles. Therefore, an integrated regulation strategy that simultaneously coordinates transport kinetics, strain accommodation, and interfacial stability is still highly needed [25].

With these considerations in mind, we focused on dimensionality reduction as a promising route for the rational design of Zn_2SnO_4-based anodes [13,18]. More importantly, dimensionality reduction here is not merely a geometric size decrease, but a controlled transformation from compact 3D particles to low-dimensional assembled architectures with reconfigured ion/electron transport pathways, stress-release modes, and surface-exposure characteristics. When further coupled with interfacial carbon confinement, such a structure is expected to promote charge transfer, shorten Li^+ diffusion length, buffer volume fluctuation, and stabilize the solid-electrolyte interphase (SEI), thereby enabling a better balance between high capacity and long-term durability [21,24]. Realizing this design, however, requires precise chemical synthesis capable of continuously regulating crystal growth, microstructural reconstruction, and surface stabilization [25,26].

Herein, we report a dimensionality-reduction-assisted structural regulation strategy for Zn_2SnO_4 anodes. Through surfactant-directed crystal growth, acid-etching reconstruction, and hydrothermal carbon coating, compact Zn_2SnO_4 octahedra are progressively transformed into sheet-assembled architectures and finally into a carbon-confined core-shell composite, denoted as C@M-Zn_2SnO_4(H^+). This structural evolution is designed to simultaneously enhance transport kinetics, relieve mechanical stress, and stabilize the electrode/electrolyte interface, while preserving the intrinsic lithium-storage mechanism of Zn_2SnO_4. The optimized C@M-Zn_2SnO_4(H^+) electrode exhibits favorable electrochemical performance, delivering 620 mAh g^{-1} after 600 cycles at 200 mA g^{-1}, with Coulombic efficiency close to 100%.

2. Materials and Methods

2.1. Materials

$SnCl_4 \cdot 5H_2O$, glucose ($C_6H_{12}O_6$), N-methyl-2-pyrrolidone (NMP), polyvinylidene fluoride (PVDF), copper foil, NaOH, lithium battery electrolyte ($LiPF_6$), Celgard separator, ethylene carbonate (EC), dimethyl carbonate (DMC), diethyl carbonate (DEC), HCl (38 wt%), HNO_3 (69 wt%), coin cell components (CR2032) were purchased from China. Ketjen black (C) was purchased from Japan. Pluronic P123 (PEO-PPO-PEO) was purchased from the USA.

2.2. Synthesis of M-Zn_2SnO_4(H^+) and C@M-Zn_2SnO_4(H^+)

In a typical synthesis, 0.4 g Pluronic P123 was dissolved in 10 mL deionized water (DIW, 18.23 MΩ) at 65 °C under ultrasonication, followed by magnetic stirring until a transparent pale-white solution was obtained. Separately, 2 mmol $ZnSO_4 \cdot 7H_2O$ and 2 mmol $SnCl_4 \cdot 5H_2O$ were dissolved in 10 mL DIW. To prevent premature coprecipitation, 2 mL concentrated HCl was added to the $SnCl_4$ solution. After 10 minutes of equilibration, the $ZnSO_4$ solution was slowly introduced into the $SnCl_4$ solution under stirring, and the mixture was stirred for an additional 20 minutes. A 2 M NaOH solution (26.75 mL) was then added using a micropump at a rate of 0.5 mL min^{-1}. The final volume was adjusted to 70 mL with DIW, and the mixture was transferred to a Teflon-lined stainless-steel autoclave, where it was heated at 200 °C for 20 h. After cooling to room temperature, the

© 2026 by the author(s). Distributed under a Creative Commons CC BY license.

Preprints.org (www.preprints.org) | NOT PEER-REVIEWED | Posted: 13 May 2026 doi:10.20944/preprints202605.0890.v1

precipitate was collected by centrifugation, washed with ethanol and DIW, and dried to obtain the precursor product.

To reconstruct the microstructure and eliminate secondary phases, the as-synthesized product was treated with 0.2 M HNO_3 for 2 h, followed by washing and drying. The resulting sample was denoted as M-$Zn_2SnO_4(H^+)$, with the untreated sample referred to as M-Zn_2SnO_4 for comparison.

For carbon-shell construction, 0.4 g of M-$Zn_2SnO_4(H^+)$ was dispersed in DIW, followed by the addition of 0.4 g of Pluronic P123 and 1 g of glucose. After hydrothermal treatment, the collected precipitate was dried and annealed in a tube furnace under flowing high-purity N_2. The sample was heated to 600 °C at a rate of 2 °C min^{-1} and held for 4 h, yielding the final gray-brown product, denoted as C@M-$Zn_2SnO_4(H^+)$.

2.3. Electrochemical Test

Electrochemical performance was evaluated using CR2032 coin cells assembled with Zn_2SnO_4-based electrodes as the working electrodes and lithium foil as both the counter and reference electrode. The active materials were mixed with Ketjen black and PVDF in NMP at a mass ratio of 8:1:1 to form homogeneous slurries. The slurries were uniformly coated onto copper foil, dried under vacuum at 100 °C for 6 h, and then punched into circular disks with a diameter of 14 mm.

Cell assembly was conducted in an argon-filled glove box with H_2O and O_2 contents below 0.1 ppm and 0.5 ppm, respectively. The electrolyte was 1.0 M $LiPF_6$ dissolved in EC, DMC, and DEC with a volume ratio of 1:1:1. Celgard 2500 membranes were used as separators. After assembly, the cells were rested for 2 h before testing.

Galvanostatic charge/discharge tests and rate-performance measurements were performed on a LAND battery testing system (model BT-2018AS, Hubei Land New Energy Equipment Co., Ltd.) at room temperature within a voltage window of 0.2-3.0 V. Cyclic voltammetry (CV) and electrochemical impedance spectroscopy (EIS) were carried out on a CHI 760e electrochemical workstation (Shanghai Chenhua Instrument Co., Ltd.). CV measurements were conducted at a scan rate of 0.2 mV s^{-1} between 0.2 and 3.0 V, starting from the open-circuit voltage. EIS measurements were performed at room temperature to evaluate interfacial charge-transfer behavior and Li^+ diffusion characteristics.

2.4. Material Characterization

X-ray diffraction (XRD) patterns were recorded on a Rigaku D/max-rB diffractometer using Cu Kα radiation over a 2θ range of 20–80° at a scanning rate of 2° min^{-1}. Raman spectra were collected on a LRS-5G-FG Raman spectrometer with a 532 nm excitation laser in the range of 200–2200 cm^{-1}. Thermogravimetric analysis (TGA) was carried out on a Mettler-Toledo simultaneous thermal analyzer at a heating rate of 5 °C min^{-1} from room temperature to 1200 °C. Morphological and microstructural features were investigated using a Nova Nano SEM450 field-emission scanning electron microscope and a Talos F200S G2 transmission electron microscope. Elemental distributions were analyzed by energy-dispersive X-ray spectroscopy (EDS), and high-angle annular dark-field (HAADF) imaging was used to further probe the microstructural characteristics of the composite samples.

3. Results

3.1. Dimensionality-Reduction-Induced Structural Evolution

By regulating the structure via dimensionality reduction, we progressively transform Zn_2SnO_4 octahedra into low-dimensional assemblies encapsulated in a carbon shell. This structural transformation shortens Li^+ transport paths, alleviates structural stress, and stabilize the electrode/electrolyte interface. As shown in Figure 1, C@M-$Zn_2SnO_4(H^+)$ was fabricated through surfactant-directed crystal growth, acid-etching induced reconstruction, hydrothermal carbon

© 2026 by the author(s). Distributed under a Creative Commons CC BY license.

Preprints.org (www.preprints.org) | NOT PEER-REVIEWED | Posted: 13 May 2026 doi:10.20944/preprints202605.0890.v1

coating, and subsequent annealing, which enables precise modulation of phase composition, microstructure, and interfacial properties.

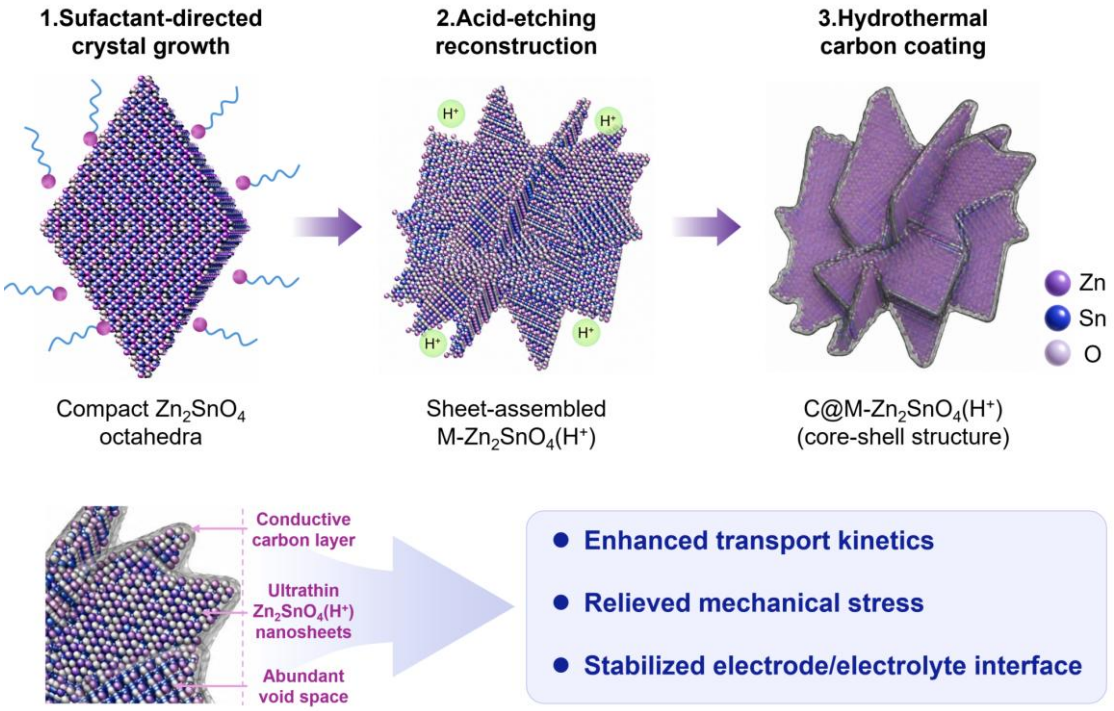

Figure 1. Schematic illustration of dimensionality reduction modulation for C@M-$Zn_2SnO_4(H^+)$.

As shown in Figure 2a, pristine Zn_2SnO_4 dispalys a well-defined regular octahedral morphology, characteristic of a compact and highly ordered three-dimensional crystal structure. Through surfactant-mediated dimensionality reduction structural modulation, the original well-defined octahedral geometry of M-Zn_2SnO_4 is disrupted, evolving instead into irregular architecture assembled from sheet-like subunits with distinct local stacking features (Figure 2b). This result indicates that the surfactant effectively modulates the nucleation pathway and preferential growth kinetics of the resultant crystals. To correlate the observed morphological transformation to its underlying phase and structural evolution, we collected X-ray diffraction (XRD) patterns (Figure 2c). All diffraction peaks of pristine Zn_2SnO_4 are indexed to the cubic inverse spinel phase (JCPDS No. 24-1470), while M-Zn_2SnO_4 retains the signature diffraction peaks of Zn_2SnO_4 phase, alongside additional peaks assignable to $ZnSnO_3$ and ZnO. This finding confirms that the surfactant both mediates the observed morphological evolution and tunes the local reaction environment and phase formation pathway during crystallization. Further acid treatment generated abundant surface pores and perforations in M-$Zn_2SnO_4(H^+)$, while completely eliminating the $ZnSnO_3$ and ZnO impurity phases (Figure 2c,d). Together, these results show that surfactant-mediated assembly followed by acid etching drives the evolution of pristine Zn_2SnO_4 from a densely packed octahedral structure into a low-dimensional porous assembly structure, thereby establishing the structural basis for high-performance LIBs.

The internal microstructure of Zn_2SnO_4-based materials was comprehensively examined using transmission electron microscopy (TEM) and high-resolution TEM (HRTEM). Compared with pristine Zn_2SnO_4, M-Zn_2SnO_4 exhibits distinct mass-thickness contrast variations in bright-field TEM images, indicating a structural evolution towards a thinner sheet-like morphology, in agreement with the scanning electron microscopy (SEM) observations (Figure S4a,b). HRTEM images of the M-Zn_2SnO_4 (Figure S4c,d) show lattice spacings of 0.24 and 0.26 nm, which we index to the (222) and (311) planes of the Zn_2SnO_4 cubic inverse spinel phase, respectively. The selected area electron diffraction (SAED) pattern reveals clear, regular diffraction spots, indicating high crystallinity and

© 2026 by the author(s). Distributed under a Creative Commons CC BY license.

Preprints.org (www.preprints.org) | NOT PEER-REVIEWED | Posted: 13 May 2026 doi:10.20944/preprints202605.0890.v1

distinct crystal orientation. In addition, the pattern is consistent with the cubic inverse spinel Zn_2SnO_4, matching well with XRD patterns.

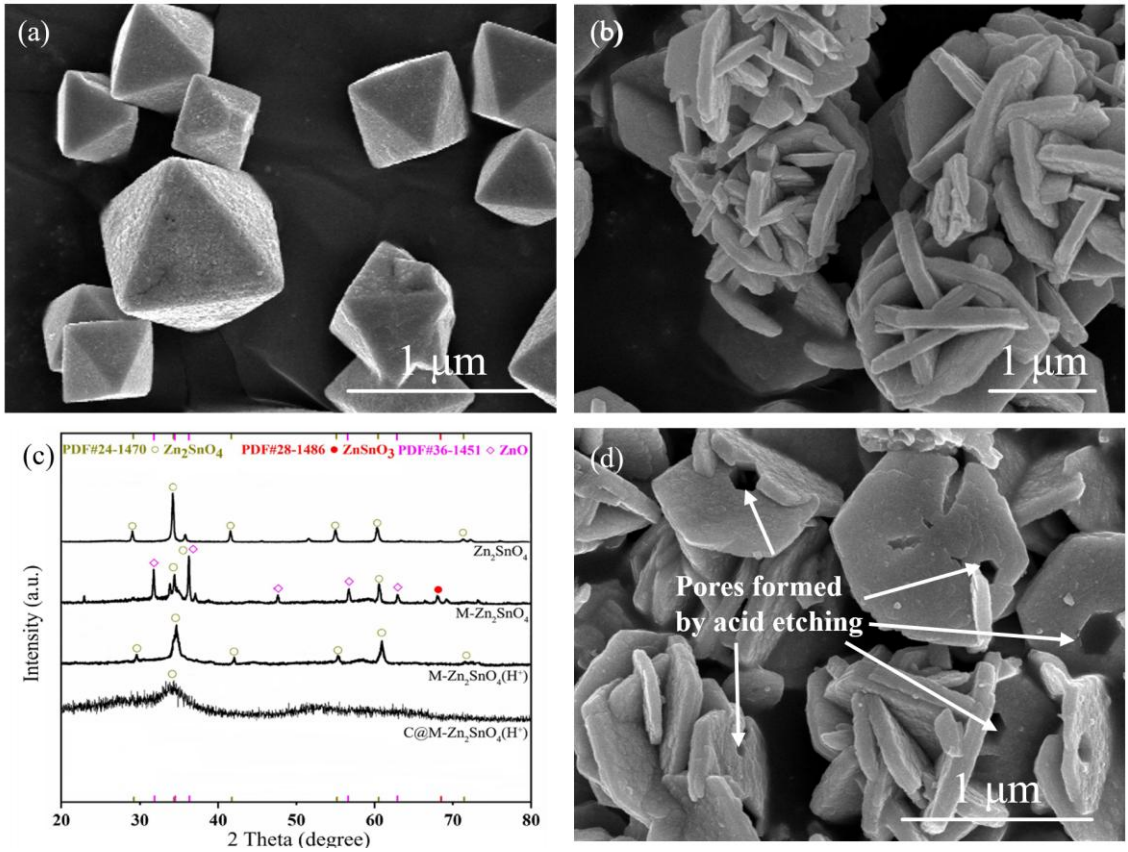

Figure 2. (**a**) SEM image of Zn_2SnO_4. (**b**) SEM image of M-Zn_2SnO_4. (**c**) XRD patterns of Zn_2SnO_4, M-Zn_2SnO_4, M-$Zn_2SnO_4(H^+)$, and C@M-$Zn_2SnO_4(H^+)$ samples. (**d**) SEM image of M-$Zn_2SnO_4(H^+)$.

Coupling carbon coating with dimensionality reduction provides a synergistic route to improved electronic/ionic transport, structural robustness and electrode/electrolyte interfaces, resulting in superior rate capability and cycling stability. We therefore hydrothermally coated M-$Zn_2SnO_4(H^+)$ with a controlled carbon layer to form a core-shell C@M-$Zn_2SnO_4(H^+)$ composite. As shown in Figure 3a–d, C@M-$Zn_2SnO_4(H^+)$ largely retains the particle morphology of the etched precursor, while a continuous shell approximately 35 nm thick is clearly observed on the surface. The absence of discernible lattice fringes in this shell indicates its amorphous carbon layer. The weak and broadened XRD diffraction peaks observed for C@M-$Zn_2SnO_4(H^+)$ can be ascribed to the shielding effect of the amorphous carbon shell surrounding the particles (Figure 2c). Elemental mapping images of C@M-$Zn_2SnO_4(H^+)$ revealed that Zn, Sn, and O are concentrated primarily in the inner region, exhibiting significant overlap, indicating that the Zn-Sn-O framework remains the structural core. In contrast, C is predominantly located on the outer surface, rather than being randomly dispersed within the bulk, confirming the core-shell structure of the C@M-$Zn_2SnO_4(H^+)$ composite (Figure 3f–j). Similar results can also be found in the SEM characterizations presented in Figure S2.

Raman spectroscopy further revealed local structural variations induced by surfactant-mediated dimensionality reduction. The characteristic Raman bands of Zn_2SnO_4 became weaker and broader after dimensionality reduction, indicating increased lattice distortion and reduced local order, consistent with the XRD results (Figure S3a). Thermogravimetric analysis further indicated a carbon content of ~13.14 wt% in C@M-$Zn_2SnO_4(H^+)$ (Figure S3b). Together, these results demonstrate the formation of a dimensionally reduced, structurally reconstructed Zn_2SnO_4-based composite with a porous oxide core and a continuous carbon shell, a configuration conducive to fast ion transport and structural stability.

© 2026 by the author(s). Distributed under a Creative Commons CC BY license.

Preprints.org (www.preprints.org) | NOT PEER-REVIEWED | Posted: 13 May 2026 doi:10.20944/preprints202605.0890.v1

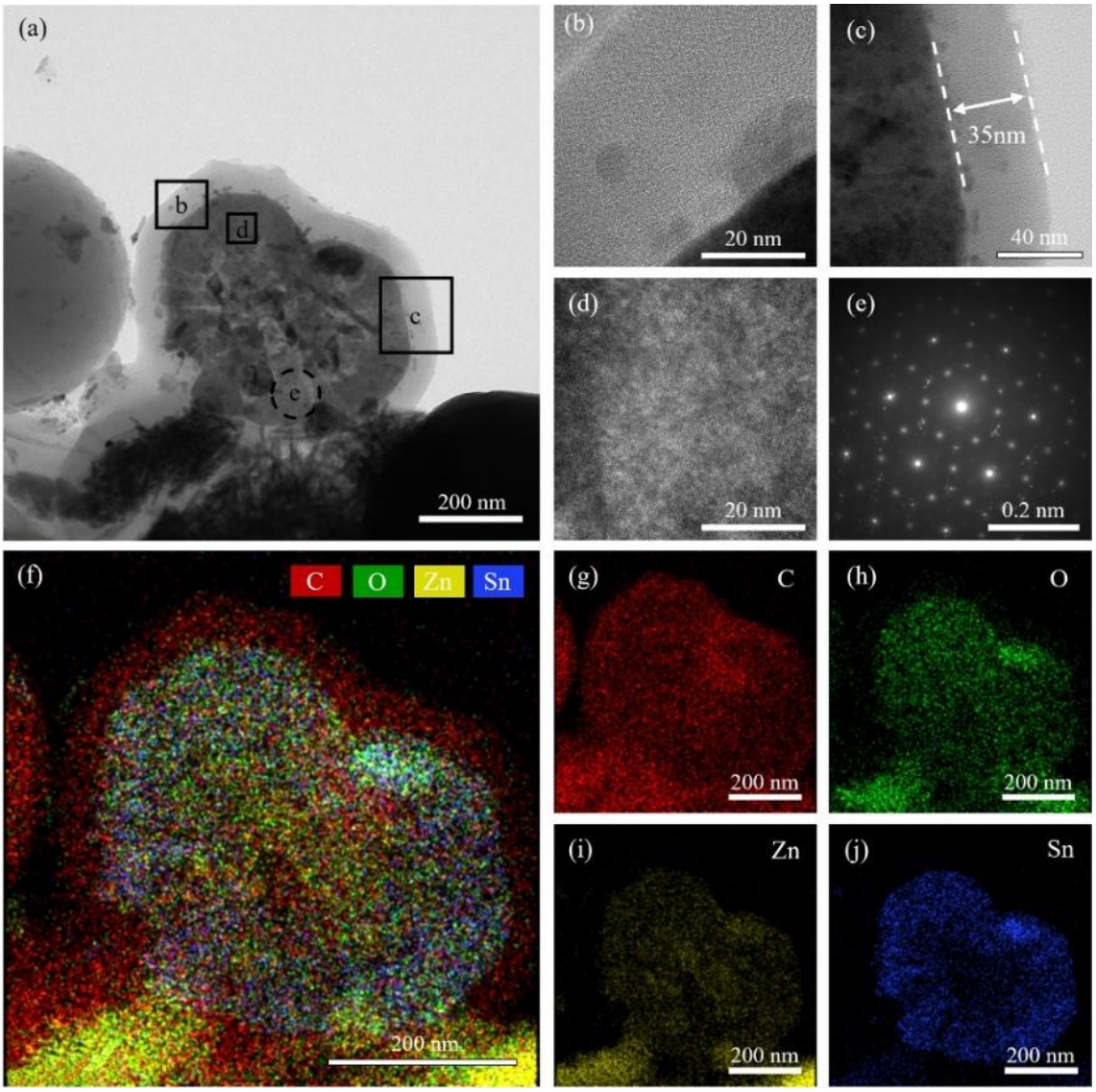

Figure 3. (**a**) TEM image of C@M-$Zn_2SnO_4(H^+)$; (**b–d**) enlarged images of different regions in (**a**). (**e**) SAED pattern of the dashed-circled region in (**a**). (**f**) overall EDS elemental mapping image of C@M-$Zn_2SnO_4(H^+)$. (**g–j**) elemental mapping images of C, O, Zn, and Sn, respectively.

3.2. Kinetic and Interfacial Effects of Structural Regulation

Electrochemical impedance spectroscopy (EIS) shows that all Zn_2SnO_4-based samples exhibit similar Nyquist plots, consisting of a semicircle in the high-frequency region and an inclined line in the low-frequency region, indicating that the electrode kinetics are jointly governed by interfacial charge transfer and Li^+ diffusion (Figure 4a). Relative to pristine Zn_2SnO_4, M-Zn_2SnO_4 displays a markedly smaller semicircle, confirming that dimensionality reduction effectively lowers the charge-transfer resistance. Following acid etching, M-$Zn_2SnO_4(H^+)$ shows a further decrease in semicircle radius together with an increased slope in the low-frequency region, suggesting improved interfacial contact and facilitated Li^+ diffusion. Notably, C@M-$Zn_2SnO_4(H^+)$ exhibits the smallest semicircle and the smallest low-frequency Warburg tail, indicative of the lowest charge-transfer resistance and optimal Li^+ diffusion kinetics among all samples. These results highlight a pronounced synergy between carbon coating and the the reconstructed framework induced by dimensionality reduction: the continuous carbon network promotes electron transport while stabilizing the electrode interface, thereby effectively mitigating polarization.

© 2026 by the author(s). Distributed under a Creative Commons CC BY license.

Preprints.org (www.preprints.org) | NOT PEER-REVIEWED | Posted: 13 May 2026 doi:10.20944/preprints202605.0890.v1

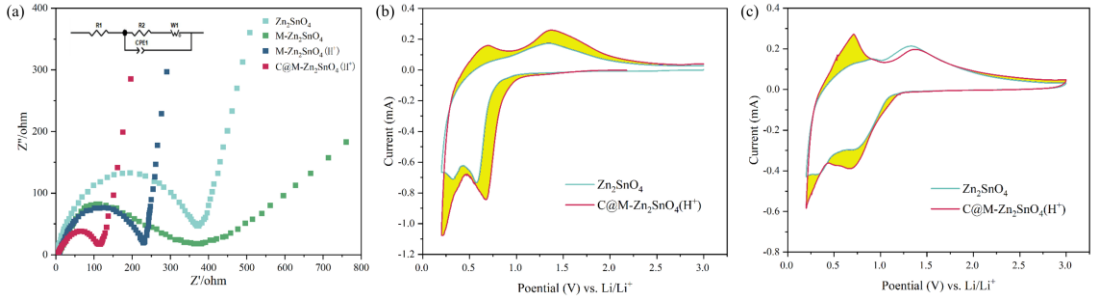

Figure 4. (**a**) Nyquist plots and the fitted equivalent circuit of Zn_2SnO_4, M-Zn_2SnO_4, M-$Zn_2SnO_4(H^+)$, and C@M-$Zn_2SnO_4(H^+)$ electrodes. (**b**) comparison of the first-cycle cyclic voltammetry curves of the Zn_2SnO_4 and C@M-$Zn_2SnO_4(H^+)$ electrodes. (**c**) comparison of the cyclic voltammetry curves of the Zn_2SnO_4 and C@M-$Zn_2SnO_4(H^+)$ electrodes during the stable cycling stage.

As shown in Figure S4, all Zn_2SnO_4-based electrodes exhibit similar redox features within 0.2-3.0 V, indicating that these electrodes follow the same intrinsic lithium-storage chemistry, namely the typical conversion reaction coupled with alloying/dealloying processes of Zn_2SnO_4-based anodes. The initial cathodic peaks in the low-potential region are associated with solid electrolyte interphase (SEI) formation, reduction of Zn_2SnO_4 to Zn/Sn and Li_2O, and the formation of Li_yZn and Li_xSn alloys, whereas the anodic peaks arise from dealloying and partial reversible conversion reactions. The discrepancy between the first and subsequent cycles reflects irreversible interfacial reactions and electrode activation.

Compared with pristine Zn_2SnO_4, the samples with dimensionality reduction modulation exhibit more defined redox peaks, improved curve overlap and reduced peak shifts, indicating enhanced reversibility and faster interfacial kinetics without altering the intrinsic reaction pathway (Figure S4). Among them, C@M-$Zn_2SnO_4(H^+)$ shows the strongest current response, largest CV area, sharpest redox peaks and smallest peak separation (Figure 4b, c), confirming reduced polarization and superior reaction kinetics enabled by the synergistic effects of dimensional regulation, acid etching and carbon coating.

3.3. Enhanced Cycling Durability and Rate Capability

We further evaluated the cycling and rate performance of the prepared electrodes. As shown in Figure 5a, the C@M-$Zn_2SnO_4(H^+)$ electrode exhibits excellent long-term cycling stability at 200 mA g^{-1}. Its discharge capacity initially stabilizes at 650 mAh g^{-1}, followed by a slight recovery after ~350 cycles, reaching ~800 mAh g^{-1}, which may arise from gradual electrode activation and microstructural rearrangement during cycling. Although gradual capacity decay occurs over prolonged cycling, the electrode still retains ~620 mAh g^{-1} after 600 cycles, with the Coulombic efficiency remaining close to 100% throughout, indicating reversible lithiation/delithiation and a stable electrode/electrolyte interface. The comparison of the first 50 cycles across all samples reveals the highest capacity retention for C@M-$Zn_2SnO_4(H^+)$, followed by M-$Zn_2SnO_4(H^+)$ and M-Zn_2SnO_4, whereas pristine Zn_2SnO_4 shows the lowest retention (Figure 5b).

© 2026 by the author(s). Distributed under a Creative Commons CC BY license.

Preprints.org (www.preprints.org) | NOT PEER-REVIEWED | Posted: 13 May 2026 doi:10.20944/preprints202605.0890.v1

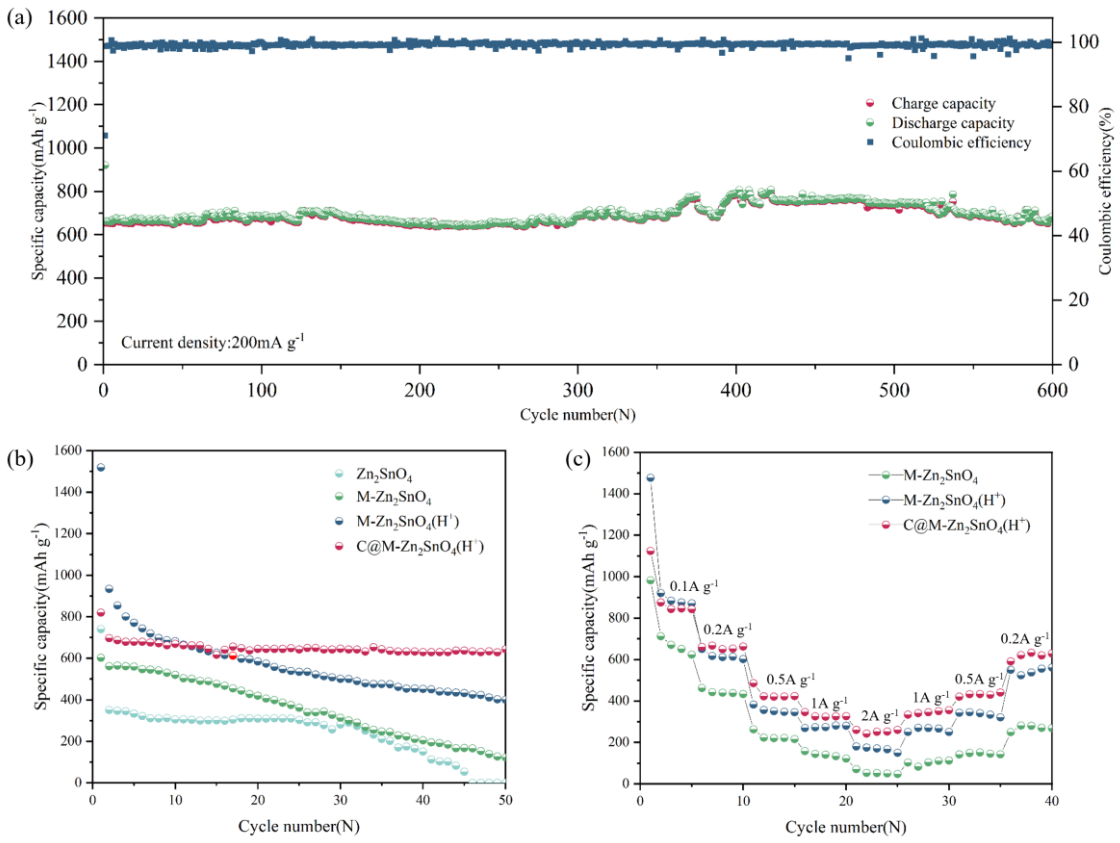

Figure 5. (**a**) Cycling performance and Coulombic efficiency of the C@M-Zn_2SnO_4(H^+) electrode at a current density of 200 mA g^{-1}. (**b**) The comparison of the cycling performance of different samples over the first 50 cycles. (**c**) rate performance of the M-Zn_2SnO_4, M-Zn_2SnO_4(H^+), and C@M-Zn_2SnO_4(H^+) electrodes.

Rate performance analysis shows that the capacities of all samples decrease progressively as the current density increases from 0.1 to 2 A g^{-1} (Figure 5c). Notably, C@M-Zn_2SnO_4(H^+) maintains higher capacities across the full current range and shows significant capacity recovery when the current returns to lower values, indicating superior rate capability and structural stability. Although M-Zn_2SnO_4(H^+) and M-Zn_2SnO_4 outperform pristine Zn_2SnO_4, their capacities and recovery capability remain inferior to those of C@M-Zn_2SnO_4(H^+). These findings further indicate that the synergistic effect between dimensionality reduction and carbon coating enhances both electronic conductivity and Li^+ transport/diffusion kinetics, thereby improving cycling stability and rate performance.

3.4. Structural Evolution of Long-Term Stability

In addition, we characterized the morphology and structure of the Zn_2SnO_4-based electrodes after extended cycling measurements to systematically assess their stability. As shown in Figure 6, after 600 cycles, the C@M-Zn_2SnO_4(H^+) electrode retains excellent surface continuity and structural integrity, with only minor micropores and slight surface deformations observed. The absence of large cracks indicates that the material retains exceptional structural stability over extended lithiation/delithiation cycles. In contrast, the pristine Zn_2SnO_4 electrode shows significant cracking after just 50 cycles, with cracks through the entire thickness dividing the electrode into irregular regions, accompanied by the precipitation of local bright impurities. This suggests severe structural degradation and interfacial instability induced by volume expansion during cycling. It is evident from these results that dimensionality reduction combined with carbon coating effectively mitigate structural damage during cycling, significantly enhancing the electrode's morphology retention.

© 2026 by the author(s). Distributed under a Creative Commons CC BY license.

Preprints.org (www.preprints.org) | NOT PEER-REVIEWED | Posted: 13 May 2026 doi:10.20944/preprints202605.0890.v1

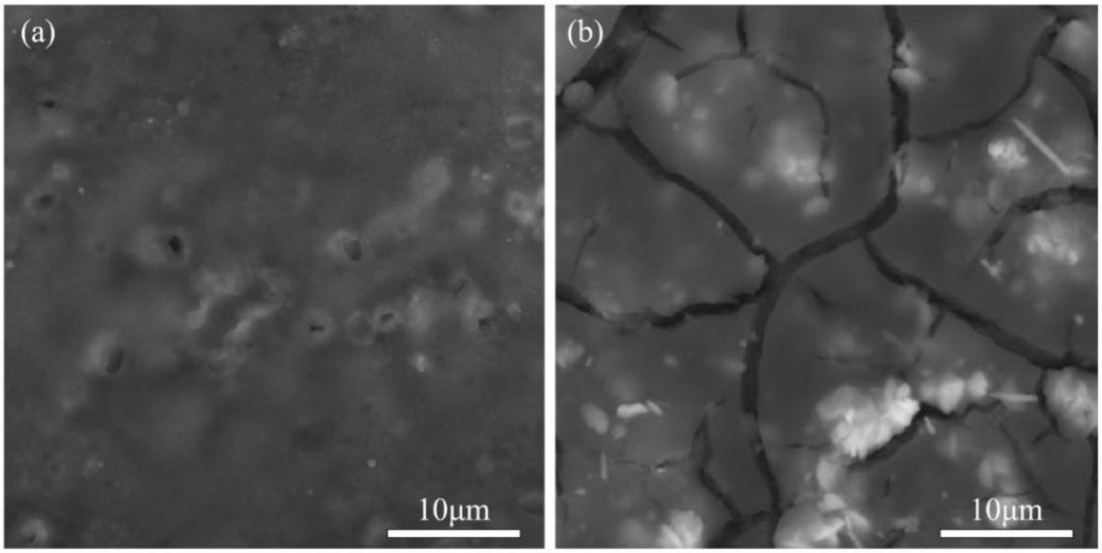

Figure 6. (**a**) SEM image of the C@M-$Zn_2SnO_4(H^+)$ electrode film after 600 cycles. (**b**) SEM image of the pristine Zn_2SnO_4 electrode film after 50 cycles.

4. Conclusions

In summary, we have transformed Zn_2SnO_4 from regular octahedral particles into a sheet-assembled core-shell composite through dimensionality reduction and carbon coating strategies, significantly enhancing the material's ion transport, electronic conductivity, and volume-buffering capabilities. The C@M-$Zn_2SnO_4(H^+)$ electrode exhibits a stable initial reversible capacity of 650 mAh g^{-1} at a current density of 200 mA g^{-1} and retains approximately 620 mAh g^{-1} after 600 cycles, with Coulombic efficiency remaining close to 100% throughout the cycling process. Morphological analysis after cycling reveals that the electrode maintains excellent surface integrity, confirming that this integrated dimensionality reduction and conductive coating strategy offers a novel approach for optimizing material structural stability, interfacial dynamics, and long-term cycling performance. This work provides a viable pathway for the development of high-performance anode materials for LIBs.

Supplementary Materials: The following supporting information can be downloaded at the website of this paper posted on Preprints.org, Figure S1: Morphological and structural characterization of M-Zn_2SnO_4; Figure S2: Elemental distribution of C@M-$Zn_2SnO_4(H^+)$; Figure S3: Raman and TGA analyses of Zn_2SnO_4-based samples; Figure S4: Cyclic voltammetry profiles of Zn_2SnO_4-based electrodes;.

Author Contributions: Zhen Meng: Investigation, Conceptualization, Formal analysis, Writing—original draft; YuanYuan Jiang: Investigation; HengLe Si: Investigation; JiCun Zheng: Methodology, Resources; HongGang Sun: Supervision, Funding acquisition; Guo-Qiang Liu: Conceived the idea, supervised the project, and co-wrote the paper. All authors discussed the results and assisted during manuscript preparation. All authors have read and agreed to the published version of the manuscript.

Funding: This research was funded by the National Natural Science Foundation of China, grant numbers 22305237 and 52471138; the Taishan Scholar Foundation of Shandong Province, grant number tsqn202408015; the Natural Science Foundation of Shandong Province, grant numbers ZR2024QE429 and ZR2023ME216; the National Key Research and Development Program of China, grant number 2021YFB3702700; and the Shenzhen Municipal Fundamental Research Program, grant number JCYJ20240813101100001.

Data Availability Statement: The original contributions presented in the study are included in the article, further inquiries can be directed to the corresponding author.

Conflicts of Interest: The authors declare no conflicts of interest.

© 2026 by the author(s). Distributed under a Creative Commons CC BY license.

Preprints.org (www.preprints.org) | NOT PEER-REVIEWED | Posted: 13 May 2026 doi:10.20944/preprints202605.0890.v1

References

1. Tarascon, J.M.; Armand, M. Issues and challenges facing rechargeable lithium batteries. Nature 2001, 414, 359-367. https://doi.org/10.1038/35104644
2. Thackeray, M.M.; Wolverton, C.; Isaacs, E.D. Electrical energy storage for transportation-approaching the limits of and going beyond, lithium-ion batteries. Energy Environ. Sci. 2012, 5, 7854-7863. https://doi.org/10.1039/C2EE21892E
3. Whittingham, M.S. Lithium batteries and cathode materials. Chem. Rev. 2004, 104, 4271-4301. https://doi.org/10.1021/cr020731c
4. Kim, T.H.; Park, J.S.; Chang, S.K.; Choi, S.; Ryu, J.H.; Song, H.K. The current move of lithium ion batteries towards the next phase. Adv. Energy Mater. 2012, 2, 860-872. https://doi.org/10.1002/aenm.201200028
5. Manthiram, A. Materials challenges and opportunities of lithium ion batteries. J. Phys. Chem. Lett. 2011, 2, 176-184. https://doi.org/10.1021/jz1015422
6. Nazri, G.A.; Pistoia, G. Lithium Batteries: Science and Technology; Springer US: New York, NY, USA, 2009.
7. Lu, J.; Chen, Z.; Pan, F.; Cui, Y.; Amine, K. High-performance anode materials for rechargeable lithium-ion batteries. Electrochem. Energy Rev. 2018, 1, 35-53. https://doi.org/10.1007/s41918-018-0001-4
8. Lee, W.W.; Lee, J.M. Novel synthesis of high performance anode materials for lithium-ion batteries (LIBs). J. Mater. Chem. A 2014, 2, 1589-1626. https://doi.org/10.1039/C3TA12830J
9. Zhong, Y.; Yang, M.; Zhou, X.; Zhou, Z. Structural design for anodes of lithium-ion batteries: Emerging horizons from materials to electrodes. Mater. Horiz. 2015, 2, 553-566. https://doi.org/10.1039/C5MH00136F
10. Ozawa, K. Lithium-ion rechargeable batteries with $LiCoO_2$ and carbon electrodes: The $LiCoO_2$/C system. Solid State Ionics 1994, 69, 212-221. https://doi.org/10.1016/0167-2738(94)90411-1
11. Poizot, P.; Laruelle, S.; Grugeon, S.; Dupont, L.; Tarascon, J.M. Nano-sized transition-metal oxides as negative-electrode materials for lithium-ion batteries. Nature 2000, 407, 496-499. https://doi.org/10.1038/35035045
12. Zhao, Y.; Li, X.; Yan, B.; Xiong, D.; Li, D.; Lawes, S.; Sun, X. Recent developments and understanding of novel mixed transition-metal oxides as anodes in lithium ion batteries. Adv. Energy Mater. 2016, 6, 1502175. https://doi.org/10.1002/aenm.201502175
13. Zhu, X.J.; Geng, L.M.; Zhang, F.Q.; Liu, Y.X.; Cheng, L.B. Synthesis and performance of Zn2SnO4 as anode materials for lithium ion batteries by hydrothermal method. J. Power Sources 2009, 189, 828-831. https://doi.org/10.1016/j.jpowsour.2008.07.028
14. Beaulieu, L.Y.; Eberman, K.W.; Turner, R.L.; Krause, L.J.; Dahn, J.R. Colossal reversible volume changes in lithium alloys. Electrochem. Solid-State Lett. 2001, 4, A137-A140.
15. Winter, M.; Besenhard, J.O. Electrochemical lithiation of tin and tin-based intermetallics and composites. Electrochim. Acta 1999, 45, 31-50. https://doi.org/10.1016/S0013-4686(99)00191-7
16. Zhou, L.; Zhang, K.; Hu, Z.; Tao, Z.; Mai, L.; Kang, Y.M.; Chou, S.L.; Chen, J. Recent developments on and prospects for electrode materials with hierarchical structures for lithium-ion batteries. Adv. Energy Mater. 2018, 8, 1701415. https://doi.org/10.1002/aenm.201701415
17. Wang, G.; Yu, M.; Feng, X. Carbon materials for ion-intercalation involved rechargeable battery technologies. Chem. Soc. Rev. 2021, 50, 2388-2443. https://doi.org/10.1039/D0CS00187B
18. Niu, C.; Meng, J.; Wang, X.; Han, C.; Yan, M.; Mai, L. Gradient-temperature hydrothermal fabrication of hierarchical Zn2SnO4 hollow boxes stimulated by thermodynamic phase transformation. J. Mater. Chem. A 2016, 4, 14095-14100. https://doi.org/10.1039/C6TA06016A
19. Kim, Y.; Kim, K.; Seo, H.; Lee, S.-M.; Park, C.-M.; Kim, J.-H. Surfactant-derived porous Sn2Nb2O7-graphene oxide composite as Li- and Na-ion storage materials. J. Alloys Compd. 2022, 910, 164943. https://doi.org/10.1016/j.jallcom.2022.164943
20. Shan, H.; Zhao, Y.; Li, X.; Xiong, D.; Dong, L.; Yan, B.; Li, D.; Sun, X. Carbon nanotubes cross-linked Zn2SnO4 nanoparticles/graphene networks as high capacities, long life anode materials for lithium ion batteries. J. Appl. Electrochem. 2016, 46, 851-860. https://doi.org/10.1007/s10800-016-0961-1
21. Kim, N.; Shim, J.-H.; Jae, W.; Song, J.; Kim, J. Zn2SnO4 particles coated with N-doped carbon as an anode material for lithium and sodium-ion batteries. J. Alloys Compd. 2019, 786, 1021-1029. https://doi.org/10.1016/j.jallcom.2019.01.370

© 2026 by the author(s). Distributed under a Creative Commons CC BY license.

Preprints.org (www.preprints.org) | NOT PEER-REVIEWED | Posted: 13 May 2026 doi:10.20944/preprints202605.0890.v1

22. Iuchi, H.; Horikawa, T.; Sotowa, K.-I.; et al. Synthesis and electrochemical performance of a nanocrystalline $Li_4Ti_5O_{12}$/C composite for lithium-ion batteries prepared using resorcinol-formaldehyde resins. Electrochim. Acta 2018, 295, 1-8. https://doi.org/10.1016/j.electacta.2018.10.188
23. Lee, D.-W.; Maulana, A.Y.; Lee, C.; Song, J.; Futalan, C.M.; Kim, J. Enhanced electrochemical performances of hollow-structured N-doped carbon derived from a zeolitic imidazole framework (ZIF-8) coated by polydopamine as an anode for lithium-ion batteries. Energies 2021, 14, 2436. https://doi.org/10.3390/en14092436
24. Yang, X.; Huang, Y.A.; Wang, M.J.; et al. Double hollow Zn2SnO4/SnO_2@N-doped carbon nanocubes as anode material for high-performance Li-ion batteries. Chem. Phys. Lett. 2023, 813, 140285.
25. Xia, J.; Tian, R.; Guo, Y.; Du, Q.; Dong, W.; Guo, R.; Fu, X.; Guan, L.; Liu, H. Zn2SnO4-carbon cloth freestanding flexible anodes for high-performance lithium-ion batteries. Mater. Des. 2018, 156, 272-277. https://doi.org/10.1016/j.matdes.2018.06.056
26. Song, W.; Xie, J.; Hu, W.; Liu, S.; Cao, G.; Zhu, T.; Zhao, X. Facile synthesis of layered Zn2SnO4/graphene nanohybrid by a one-pot route and its application as high-performance anode for Li-ion batteries. J. Power Sources 2013, 229, 6-11. https://doi.org/10.1016/j.jpowsour.2012.11.090
27. Bao, L.H.; Zang, J.F.; Wang, G.F.; Li, X. Atomic-scale imaging of cation ordering in inverse spinel Zn2SnO4 nanowires. Nano Lett. 2014, 14, 6505-6509. https://doi.org/10.1021/nl503077y
28. Dou, J.; Chen, Q. Zinc stannate nanostructures for energy conversion. Chin. J. Chem. 2021, 39, 367-380. https://doi.org/10.1002/cjoc.202000369
29. Naraprawatphong, R.; Chokradjaroen, C.; Thiangtham, S.; Yang, L.; Saito, N. Nanoscale advanced carbons as an anode for lithium-ion battery. Mater. Today Adv. 2022, 16, 100290.
30. Liang, S.; Cheng, Y.-J.; Zhu, J.; Xia, Y.; Müller-Buschbaum, P. A chronicle review of nonsilicon (Sn, Sb, Ge)-based lithium/sodium-ion battery alloying anodes. Small Methods 2020, 4, 2000218. https://doi.org/10.1002/smtd.202000218

Disclaimer/Publisher's Note: The statements, opinions and data contained in all publications are solely those of the individual author(s) and contributor(s) and not of MDPI and/or the editor(s). MDPI and/or the editor(s) disclaim responsibility for any injury to people or property resulting from any ideas, methods, instructions or products referred to in the content.

© 2026 by the author(s). Distributed under a Creative Commons CC BY license.